

Arbitrary linear transformations for photons in the frequency synthetic dimension

Siddharth Buddhiraju, Avik Dutt, Momchil Minkov, Ian A. D. Williamson, and Shanhui Fan
 Ginzton Laboratory, Department of Electrical Engineering,
 Stanford University, Stanford, California 94305, USA
 (Dated: September 7, 2020)

Arbitrary linear transformations are of crucial importance in a plethora of photonic applications spanning classical signal processing, communication systems, quantum information processing and machine learning. Here, we present a new photonic architecture to achieve arbitrary linear transformations by harnessing the synthetic frequency dimension of photons. Our structure consists of dynamically modulated micro-ring resonators that implement tunable couplings between multiple frequency modes carried by a single waveguide. By inverse design of these short- and long-range couplings using automatic differentiation, we realize arbitrary scattering matrices in synthetic space between the input and output frequency modes with near-unity fidelity and favorable scaling. We show that the same physical structure can be reconfigured to implement a wide variety of manipulations including single-frequency conversion, nonreciprocal frequency translations, and unitary as well as non-unitary transformations. Our approach enables compact, scalable and reconfigurable integrated photonic architectures to achieve arbitrary linear transformations in both the classical and quantum domains using current state-of-the-art technology.

INTRODUCTION

Arbitrary linear transformations in photonics [1–3] are of central importance for optical quantum computing [4], classical signal processing and deep learning [5–10]. A variety of architectures are being actively studied to implement linear transformations for quantum computation and photonic neural networks, including those based on Mach-Zender interferometers (MZI) [4, 5], microring weight banks [6, 7, 11], phase-change materials [8, 9], and diffractive metasurfaces [10]. All such approaches use path encoding of photons in real space. By contrast, implementing such linear transformations in the frequency space would open avenues beyond those possible with previously reported architectures, which are inherently time-invariant. For example, frequency-space transformations allow spectrotemporal shaping of light and generation of new frequencies, with wide-ranging applications in frequency metrology, spectroscopy, communication networks, classical signal processing [12–14] and linear optical quantum information processing [15–24]. Nonlinear optics has traditionally been the workhorse for such spectrotemporal shaping, but the requirement of high-power fields and the difficulty of implementing *arbitrary* linear transformations motivates new architectures for manipulating states in the frequency domain. To that end, photonic synthetic dimensions offer an attractive solution to implement linear transformations in a single physical waveguide by harnessing the internal degrees of freedom of a photon [25–32]. Synthetic frequency dimensions in particular offer a small spatial footprint and inherent reconfigurability since multiple frequency modes can be addressed simultaneously, and the short- and long-range coupling [29, 30, 33, 34] between them can be controlled by applying an appropriate time-domain signal to a modulator.

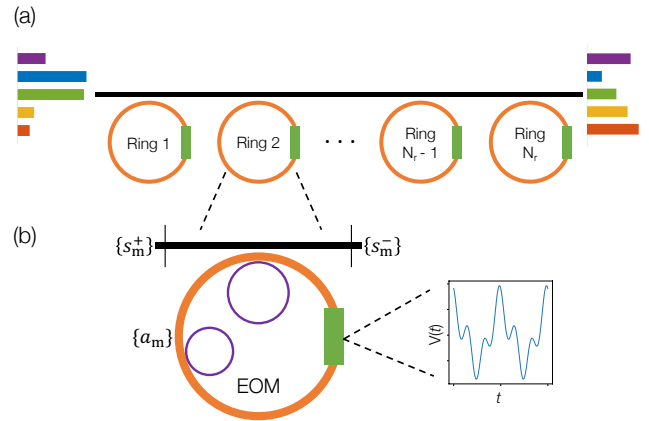


FIG. 1. (a) Schematic of an array of dynamically modulated rings (orange) coupled to an external waveguide in order to achieve arbitrary linear transformations in frequency space. The green blocks represent electro-optic modulators (EOMs) and the black line is an external waveguide coupling to each of the rings. The output spectrum on the right is the result of the transformation implemented by the system on the input spectrum (left). (b) Detailed view of a single ring depicting the waveguide port inputs and outputs s_m^\pm . The smaller purple circles indicate auxiliary rings that couple selectively to modes a_m of the larger orange ring to implement frequency-dimension truncation to the ring spectrum. The time-periodic voltage profile applied to the EOM is a result of the inverse-design algorithm.

Here, we show that arbitrary linear transformations can be performed directly in the synthetic space spanned by the different frequency modes carried by a single physical waveguide. We use gradient-based inverse design to automate the process of designing the linear transformations, and demonstrate that a wide variety of transformations can be realized. As examples, we show single frequency conversion, nonreciprocal frequency transla-

tions as well as general arbitrary unitary and non-unitary transformations, all achieved with high fidelities in a fully reconfigurable fashion.

Our work is in contrast to previous works where different frequency channels were used in parallel but without frequency conversions among them [6, 7, 9, 11] by demultiplexing the different frequencies into separate spatial channels. Additionally, optimized fast modulation has been used for tailoring single photon spectra from two-level quantum emitters [35], or for quantum frequency conversion [15] and linear optical quantum computation [17, 36], where the modulator is used as a generalized beam splitter in synthetic frequency dimensions. However, the design of an entire scattering matrix that implements an arbitrary $N \times N$ linear transformation in synthetic space, which is essential for many applications in quantum information processing and neural networks, is unique to our work.

THEORY

Consider a ring of radius R formed by a single mode waveguide with a refractive index n . The ring is coupled to an external waveguide of the same refractive index. Assuming sufficiently weak coupling between the ring and the external waveguide and neglecting group-velocity dispersion, the eigenmodes of the ring occur at frequencies $\omega_m = \omega_0 + m\Omega_R$, where ω_0 is the central frequency, m is an integer and $\Omega_R = c/nR$ is the free spectral range (FSR) of the ring with c being the speed of light in vacuum. These eigenmodes take the form $e^{-i(m_0+m)\phi}$, where m_0 denotes the angular momentum of the 0th mode and ϕ is the azimuthal coordinate of the ring. Corresponding to these eigenmodes, we define $a_m(t)e^{i\omega_m t}$ to be the amplitude of the mode centered at ω_m , normalized such that $|a_m(t)|^2$ corresponds to the photon number in the m th mode. Likewise, we define $s_m^\pm(t)e^{i\omega_m t}$ to be the amplitudes of the modes of the external waveguide at the input and output ports, respectively, as shown in Fig. 1(b). The coupling between the ring modes and waveguide modes at frequency ω_m is described by an external coupling rate γ_m^e , while other losses occurring in the ring, such as absorption or bending loss, are captured by an internal decay rate γ_m^i . Lastly, we assume that the dielectric constant of the ring is modulated using an electro-optic modulator in the form $\sum_{l=1}^{N_f} \delta\epsilon_l(\phi) \cos(l\Omega_R t + \theta_l)$, where $\delta\epsilon_l$ is the depth of the modulation and θ_l is the phase of the modulation at frequency $l\Omega_R$. The angular dependence $\delta\epsilon_l(\phi)$ occurs due to the physical localization of the electro-optic modulator to a specific range of ϕ , as shown in Fig. 1. The dynamics of the coupled ring-waveguide system can be described by a coupled-mode

theory (see Supplementary Material, Sec. I) given by:

$$-id_t a_m = i(\gamma_m^e + \gamma_m^i) a_m + \sqrt{2\gamma_m^e} s_m^+ + \sum_{l=1}^{N_f} (\kappa_l a_{m-l} + \kappa_{-l} a_{m+l}), \quad (1)$$

$$s_m^- = s_m^+ + i\sqrt{2\gamma_m^e} a_m, \quad (2)$$

where

$$\kappa_{\pm l} = -\frac{\alpha_l}{4n^2} e^{\mp i\theta_l} \int_0^{2\pi} e^{\mp il\phi} \delta\epsilon_l(\phi) d\phi \quad (3)$$

is the modulation-induced coupling between the modes of the ring, with α_l describing the radial and zenith-angle overlap of the eigenmodes of the ring with the electro-optic modulator (see Supplementary Material, Sec. I).

If the $\delta\epsilon_l$'s are real, i.e., only the real part of the refractive-index is modulated, then $\kappa_l^* = \kappa_{-l}$. Therefore, the modulation conserves the total photon number summed across all frequency channels. Further, if γ_m^i are negligible, then no photons are lost to absorption or radiation. Under these conditions, the setup of Eqs. (1)-(2) implements a unitary transformation between the fields s_m^+ at the input ports and the fields s_m^- at the output ports. This unitary transformation can be obtained by first converting Eq. (1) to the frequency domain, resulting in

$$\mathbf{a} = [\Delta\omega - i\Gamma - \mathcal{K}]^{-1} \sqrt{2\Gamma} \mathbf{s}^+, \quad (4)$$

where $\mathbf{a} = \{\dots a_{-1}, a_0, a_1, \dots\}^t$, $\mathbf{s}^\pm = \{\dots s_{-1}^\pm, s_0^\pm, s_1^\pm, \dots\}^t$, $\Gamma = \text{diag}(\dots \gamma_{-1}^e, \gamma_0^e, \gamma_1^e, \dots)$, $\Delta\omega$ is a constant detuning of the equally-spaced frequencies of input comb \mathbf{s}^+ from the ring's resonant frequencies, and $\mathcal{K}_{mm'} \equiv \kappa_{m-m'}$ as defined by Eq. (3). Then, from Eq. (2), we obtain $\mathbf{s}^- = \mathcal{M} \mathbf{s}^+$, where

$$\mathcal{M} = \left[\mathcal{I} + i\sqrt{2\Gamma} [\Delta\omega - i\Gamma - \mathcal{K}]^{-1} \sqrt{2\Gamma} \right]. \quad (5)$$

A direct verification of the unitarity of \mathcal{M} is included in the Supplementary Material (Sec. II). In the idealized situation as described above, where the ring-waveguide system is assumed to be single-moded over a broad bandwidth and is free from group velocity dispersion, the matrix \mathcal{M} is infinite-dimensional. In practice, the dimensionality of the scattering matrix can be controlled by introducing a ‘‘truncation’’ along the frequency dimension. Such a truncation can be implemented using one or more auxiliary rings coupled to the main ring (see Supplementary Material, Sec. III). The auxiliary rings couple to and perturb a few modes immediately outside the $(2N_{\text{sb}} + 1)$ modes around the 0th mode, dispersively shifting and splitting them. These perturbed modes have frequencies such that the

modulation tones of $l\Omega_R$ cannot couple these modes to the $(2N_{\text{sb}} + 1)$ modes of interest. Therefore, the total number of modes under consideration in the coupled ring-waveguide system is $2N_{\text{sb}} + 1$, and the scattering matrix defined in Eq. (5) is of size $(2N_{\text{sb}} + 1) \times (2N_{\text{sb}} + 1)$.

The main objective of our paper is to show that an arbitrary scattering matrix of size $(2N_{\text{sb}} + 1) \times (2N_{\text{sb}} + 1)$ can be created. To that end, we first note that the number of real degrees of freedom in the scattering matrix (Eq. (5)) of a single ring under modulation is equal to twice the number of distinct modulation tones, $2N_f$, provided the modulation amplitudes $\delta\epsilon_l$ and phases θ_l are independently controllable. Since the system is truncated to have $2N_{\text{sb}} + 1$ frequencies, the largest harmonic of Ω_R that will result in nonzero coupling between any two modes is $2N_{\text{sb}}$, i.e., $N_f \leq 2N_{\text{sb}}$. Since an arbitrary unitary matrix of size $(2N_{\text{sb}} + 1) \times (2N_{\text{sb}} + 1)$ has $(2N_{\text{sb}} + 1)^2$ real degrees of freedom whereas $N_f \leq 2N_{\text{sb}}$, we conclude that a single modulated ring is insufficient to approximate an arbitrary unitary matrix to a high degree of accuracy, even if all modulation tones up to $2N_{\text{sb}}\Omega_R$ are used. To overcome this problem, notice that products of unitary transformations are also unitary [37]. Therefore, as shown in Fig. 1(a), instead of a single ring, we consider a sequence of N_r number of rings with each ring providing N_f complex degrees of freedom. Thus, if the total degrees of freedom in series of rings coupled to the waveguide, given by $2N_f N_r$, exceeds $(2N_{\text{sb}} + 1)^2$, then the setup of Fig. 1(a) should be able to approximate an arbitrary unitary transformation to a high degree of accuracy.

Below, we optimize these $2N_f N_r$ degrees of freedom to enable physical approximation of arbitrary unitary and certain non-unitary transformations. For unitary transformations or parts thereof, we use as the objective function the fidelity, which measures the accuracy of an approximation V to a unitary transformation U :

$$\mathcal{F}(U, V) = \frac{|\langle U, V \rangle|}{\sqrt{\|U\|_F \|V\|_F}}, \quad (6)$$

where $\langle U, V \rangle = \sum_{ij} U_{ij}^* V_{ij}$ is the element-wise inner product and $\|U\|_F = \sqrt{\sum_{ij} |U_{ij}|^2}$ is the Frobenius norm. The use of an absolute value in Eq. (6) allows for the tolerance of a single global phase, i.e., if $f(U, V) = 1$, then the transformation V achieved by the architecture is equal to $Ue^{i\Phi}$ for some phase Φ . To achieve a high fidelity for a given target matrix we use gradient-based inverse design to optimize the parameters of the modulated system. To enable such optimization, we implemented a numerical model of the unitary transformations defined by Eq. (5) in an automatic differentiation framework [38]. While explicitly defined adjoint variable methods have been widely used for photonic inverse

design [39], automatic differentiation is the generalization of the adjoint variable methods to arbitrary computational graphs. Automatic differentiation has recently been successfully applied to the inverse design of photonic band structures [40] as well as photonic neural networks [41], where explicit adjoint methods are challenging to implement. Here, automatic differentiation enables the efficient computation of the gradients of a scalar objective function with respect to complex control parameters, which in this case are the coupling constants $\kappa_{\pm l}$ as defined in Eq. (3). The advantage of using automatic differentiation is that one needs only to implement the computational model as described above, while the automatic differentiation framework manages the gradient computation through an efficient reverse-mode differentiation. Using the gradients from automatic differentiation, the Limited-memory Broyden-Fletcher-Goldfarb-Shanno (LBFGS) algorithm [42] is used for optimization.

RESULTS

For the results in this section, we assume that the ring-waveguide system under consideration operates with $N_{\text{sb}} = 2$, i.e., 5 equally-spaced lines followed by at least 4 perturbed lines on each side. The five relevant modes are indexed $\{-2, -1, 0, 1, 2\}$. For simplicity, we assume that all five ring modes couple to the waveguide with equal strength, i.e., $\gamma_m^e \equiv \gamma \forall m$. We also assume that the source frequencies in the waveguide are on resonance with the ring, i.e., $\Delta\omega = 0$ in Eq. (5). Note that under these assumptions, the transformations in Eq. (5) are completely determined by the ratios κ_l/γ .

First, we consider the application of such ring-waveguide networks to implement high-fidelity frequency translation that is useful for frequency-domain beam splitters or single-qubit gates. As an example, we show a design where an input signal in mode 0, after forward propagation through the network, results in a complete conversion to mode +2. Using our inverse-design framework, such a frequency translation corresponds to designing only one column of a unitary transformation and can be achieved with a fidelity exceeding 99.999% using just two rings and two modulation tones per ring, as shown in Fig. 2(a)-2(b). In Fig. 2(c), we present the error function versus the number of iterations. The error function is defined as $1 - F_{+2}$, where F_{+2} is the normalized output photon flux in the mode +2. After a few iterations, almost all the photon flux is converted to frequency ω_{+2} at the output.

In addition to such high-fidelity frequency conversion implemented in forward propagation through the network, the transformations achieved in this architecture can be different in forward and reverse propagation due

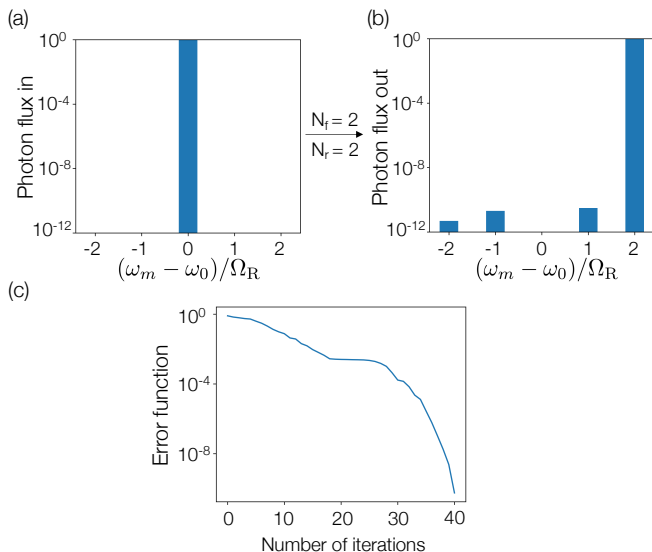


FIG. 2. A two-ring system ($N_r = 2$) with two modulation tones per ring ($N_f = 2$) demonstrating over 99.999% conversion efficiency from mode 0 to +2. The bar plots show log-scale photon flux in each mode at (a) the input, and (b) the output. (c) The error function as a function of the number of iterations of the optimization algorithm to achieve the conversion efficiency of (b). Modulation parameters are provided in the Supplementary Material (Sec. IV).

to the relative phase shift between the modulation tones across the different rings and the explicit time-varying nature of the dynamically modulated system [43]. This is in sharp contrast with MZI-based architectures, which are inherently reciprocal. As an example, we show in Fig. 3 that we can simultaneously realize with a fidelity exceeding 99.999% a frequency shift, say, $0 \rightarrow 2$, in forward propagation (Fig. 3(a)) and a different shift, say, $2 \rightarrow 1$, in reverse propagation (Fig. 3(b)) with three modulated rings.

Achieving frequency shifts using modulated rings, as shown in Fig. 2 and Fig. 3, requires designing only one and two columns of the 5×5 unitary matrix, respectively. On the other hand, if the number of modulation tones N_f and/or the number of rings N_r are increased, an arbitrary unitary transformation can be achieved with a high fidelity. As an example, we depict in Fig. 4(a) a 5×5 permutation matrix U , defined by $U_{21} = U_{32} = U_{43} = U_{54} = U_{15} = 1$, and zero otherwise. In Fig. 4(b), we present the amplitudes of the matrix achieved using one ring and three modulation tones, resulting in a fidelity of 92.03%. With just one ring but four modulation tones, the fidelity is boosted to over 99.999%, as shown by the amplitudes in Fig. 4(c). In Fig. 4(d), we tabulate as a function of N_r and N_f the maximum fidelity obtained in approximating the 5×5 permutation matrix, showing that a fidelity exceeding 99% can be achieved using a wide variety of N_r and N_f combinations.

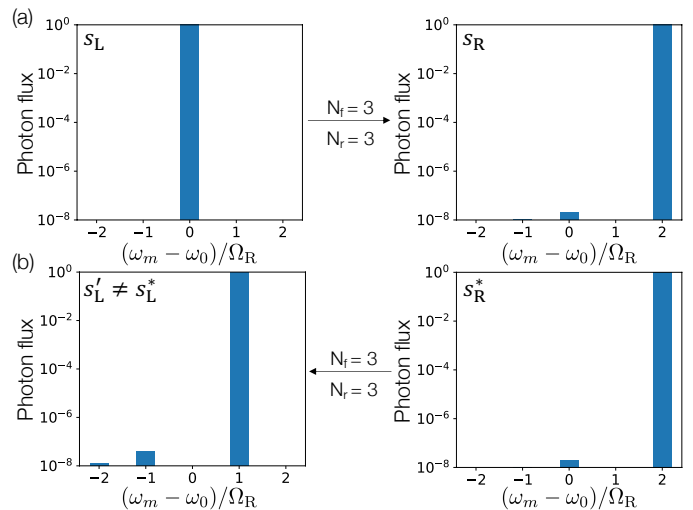


FIG. 3. A three-ring system with three modulation tones per ring demonstrating (a) 99.999% conversion efficiency from mode 0 to mode +2 in forward propagation. The input and output field profiles are indicated by s_L and s_R , respectively. (b) The *complex-conjugated* output profile, s_R^* , injected back into the output port results in a 99.999% conversion efficiency from mode +2 to +1 instead of mode 0 in backward propagation through the same system, indicating highly efficient nonreciprocal frequency shifts. Modulation parameters are provided in the Supplementary Material (Sec. IV).

In Fig. 4, we considered only the accuracy of the amplitudes achieved by our inverse-design approach. We now show that our architecture can also capture the phase of an arbitrary unitary transformation with a high fidelity. To demonstrate this, we consider a normalized 5×5 Vandermonde matrix, which is used to implement the discrete Fourier transform. This unitary transformation, defined by $U_{mn} = e^{-2\pi imn/5}/\sqrt{5}$, has a constant amplitude across its matrix elements but significantly varying phase, as shown in Fig. 5(a). With the use of one ring and four modulation tones, the inverse-design algorithm is able to achieve a fidelity of 79.999%, with the corresponding phase profile shown in Fig. 5(b) up to a global phase of 0.0099π . As depicted in Fig. 5(c), a significantly better performance is possible with the use of 4 rings and 4 modulation tones per ring, achieving a fidelity exceeding 99.999% with a global phase of 0.596π . A map of maximum fidelities achieved by our inverse design approach as a function of the number of rings and modulation tones is shown in Fig. 5(d).

While unitary transformations are usually required for quantum information processing, matrices used in classical signal processing and in neural networks are in general non-unitary. The architecture presented thus far can also be used to implement non-unitary matrices with sin-

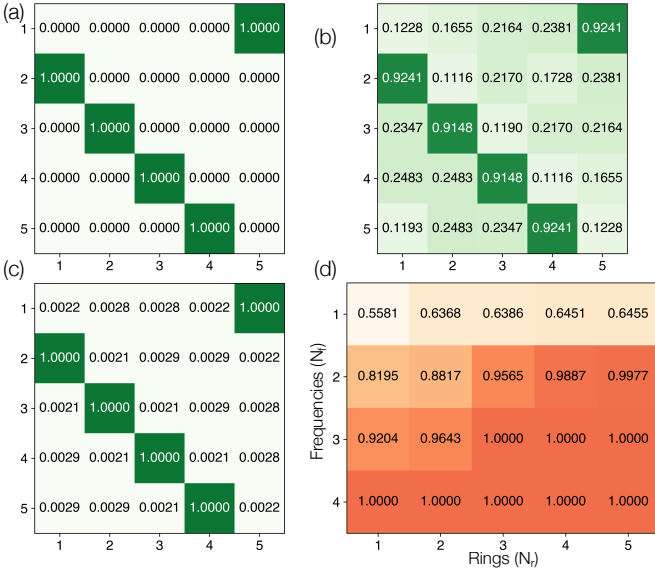


FIG. 4. (a) A 5×5 permutation matrix to be implemented by the ring-waveguide system. The amplitudes of the matrix elements are indicated along with a green colormap. (b) Element-wise amplitudes of the optimized result using one ring ($N_r = 1$) and (b) three modulation tones ($N_f = 3$), achieving a 92.03% fidelity, and (c) four modulation tones ($N_f = 4$), achieving a fidelity exceeding 99.999%. (d) Maximum fidelities reported by the inverse-design algorithm as a function of N_r and N_f . An entry of 1.0000 indicates a fidelity exceeding 99.995%. Modulation parameters for (c) are provided in the Supplementary Material (Sec. IV).

gular values less than or equal to one using one of two techniques. First, such non-unitary matrices can provably be embedded in larger unitary matrices [44] using their singular value decomposition. Subsequently, the larger unitaries can be implemented using refractive index modulation as discussed thus far. As an example, we consider the following 3×3 non-unitary matrix that was randomly generated subject to the constraint that its largest singular value is equal to one:

$$M = \begin{pmatrix} 0.4993e^{i0.2483\pi} & 0.3135e^{i0.3251\pi} & 0.3150e^{i0.1519\pi} \\ 0.2580e^{i0.4129\pi} & 0.2888e^{i0.1608\pi} & 0.4420e^{i0.0492\pi} \\ 0.5277e^{i0.2319\pi} & 0.2382e^{i0.1053\pi} & 0.1992e^{i0.4087\pi} \end{pmatrix}.$$

The singular values of M are 1, 0.3755 and 0.1421, respectively. Since there are two singular values less than 1, M can be extended into a unitary matrix by adding two dimensions. The element-wise amplitude and phase corresponding to the extended 5×5 unitary matrix are shown in Fig. 6(a) and Fig. 6(c), respectively. Using four rings ($N_r = 4$) and four modulation tones per ring ($N_f = 4$), our inverse-design algorithm achieves the extended unitary matrix with a fidelity exceeding 99.999%, as shown in Fig. 6(b) and Fig. 6(d). Notice that the phase of element (5,4) is significantly different between Fig. 6(c) and Fig. 6(d), but this is because the target amplitude for this element is zero. As an alterna-

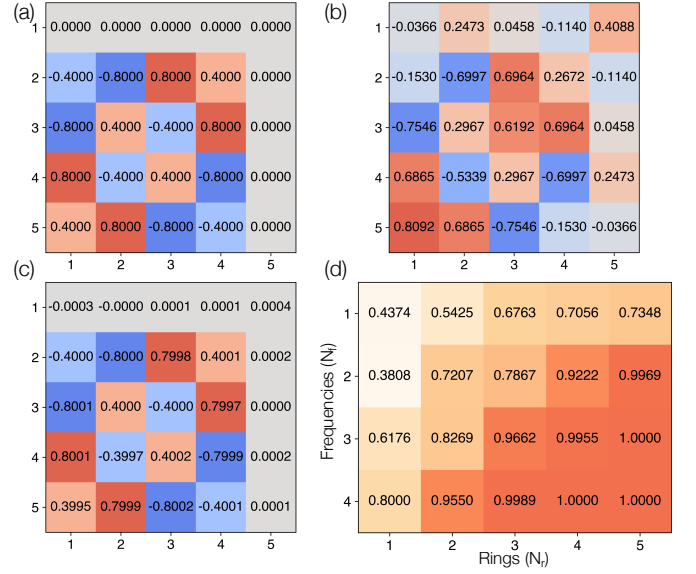


FIG. 5. Element-wise phase as a fraction of π of the 5×5 Vandermonde matrix implementing the discrete Fourier transform. Element-wise phase achieved by the inverse-design algorithm for (b) $N_r = 1$ and $N_f = 4$, with a fidelity of 79.999% and global phase of 0.099π and (c) $N_r = 4$ and $N_f = 4$, with a fidelity of 99.999% and global phase 0.596π . (d) Maximum fidelities reported by the inverse-design algorithm as a function of N_r and N_f . Modulation parameters for (c) are provided in the Supplementary Material (Sec. IV).

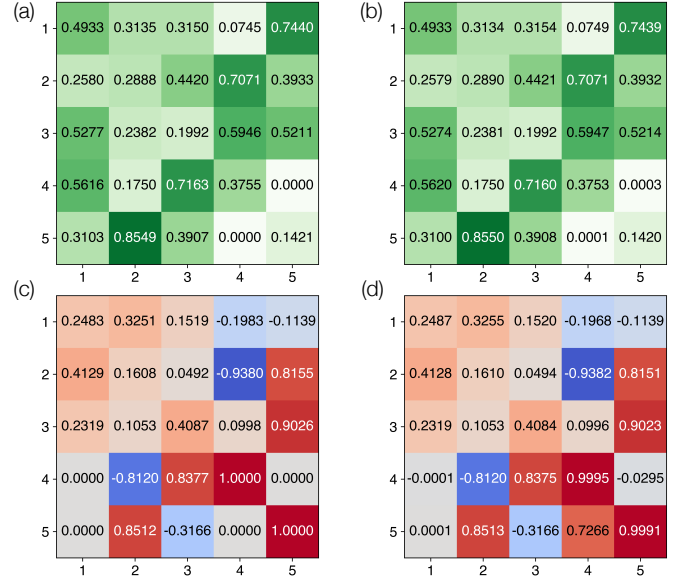


FIG. 6. Achieving non-unitary transformations by embedding in a larger unitary matrix. The target non-unitary matrix, located in the upper-left 3×3 section of the matrix, is first extended to a unitary 5×5 target matrix. The element-wise (a) target amplitude, (b) achieved amplitude, (c) target phase, and (d) achieved phase as a fraction of π are shown. A near ideal implementation was achieved using $N_r = 4$ and $N_f = 4$ with a fidelity exceeding 99.999%. Modulation parameters are provided in the Supplementary Material (Sec. IV).

tive approach, amplitude modulation, where the imaginary part of the refractive index is also modulated, can also be used to directly implement non-unitary matrices since the transformation of Eq. (5) is non-unitary under modulation of the imaginary part of the refractive index. Lastly, in order to implement matrices with singular values greater than 1, a gain element is necessary. For such matrices, a scaled version such that the singular values are below 1 can first be implemented using the methods outlined above, after which a uniform amplification for all frequency channels can rescale the matrix to its intended form.

DISCUSSION

We have shown that combining the concepts of synthetic dimensions and inverse design enables the implementation of versatile linear transformations in photonics. A major advantage of using synthetic frequency dimensions for implementing an $N \times N$ linear transformation is that only $O(N)$ photonic elements (modulators in our case) need to be electrically controlled. This is in contrast to real-space dimensions using path-encoding, such as MZI meshes or crossbar arrays, where the full $O(N^2)$ degrees of freedom need to be electrically controlled. Such control is nontrivial both from a scalability perspective as well as from a practical geometrical perspective of connecting N^2 tunable elements (e.g. phase-shifters) to their driving electronics off-chip. The reduction in the number of individually controlled elements from $O(N^2)$ to $O(N)$ in our scheme comes from the fact that the driving signal on each of the N_r EOMs can simultaneously address N_f frequency modes in the synthetic dimension.

Future work could leverage synthetic frequency dimensions for complicated quantum information protocols beyond single-qudit unitary transformations, such as realizing probabilistic entangling gates for linear optical quantum computing (LOQC) [17, 36]. In particular, spectral LOQC using EOMs and pulse shapers has been shown to be universal for quantum computation [17]. However, pulse shapers involve demultiplexing the frequency modes into distinct spatial channels using gratings to apply mode-by-mode phase shifts, and limit the number of modes that can be accommodated within the modulator bandwidth due to a finite spectral resolution, thus reducing the benefit of using synthetic frequency dimensions. Such pulse shapers are also lossy and challenging to integrate on chip. Our architecture obviates the pulse shaper by exclusively using EOMs. The advent of ultralow-loss nanophotonic EOMs in lithium niobate [45, 46], as well as progress in silicon [47, 48] and aluminum nitride [49] makes our architecture fully compatible with on-chip integration, since modulation at frequencies exceeding the ring's FSR have been demonstrated [14, 47, 50].

For applications in neural networks, the performance of our architecture in terms of the speed, compute density and energy consumption for multiply-and-accumulate (MAC) operations is important [51]. Assuming we need N modulation tones and N rings with FSR $\Delta f = \Omega_r/2\pi$ to implement a matrix, we can input information encoded in the N frequencies and read out the matrix-vector product, which amounts to N^2 MAC operations. Since we need a frequency-resolved measurement, the fastest readout bandwidth is Δf . We assume that the input data can be prepared at speed comparable to or faster than the readout speed. Then, the computational speed in MACs per second is given by

$$C = N^2 \Delta f. \quad (7)$$

The maximum number of channels is limited by the FSR and the modulation bandwidth. If we utilize the whole available bandwidth, $B = N \Delta f$, then the speed is

$$C = NB. \quad (8)$$

For a modulation bandwidth of 100 GHz and an FSR of 100 MHz (such that $N = 1,000$), this yields a speed $C = 10^{14}$ MACs/s or 100 TMAC/s, which is comparable with MZI meshes [5, 51, 52]. Although achieving such small FSRs on chip is challenging, recent progress in integrating low-loss delay lines on chip [53, 54] holds promise, since meter-scale delays were reported in an 8 mm² footprint using spiral resonators, corresponding to an equivalent FSR of ~ 350 MHz [53]. These design techniques can be extended to lithium niobate rings with high modulation bandwidths [14, 46].

To optimize for computation density, i.e. MACs/s per unit area [51], one can use a larger FSR $\Delta f = 1$ GHz, in a 1-mm² footprint, and combine synthetic frequency dimensions within each 100-GHz modulation bandwidth with wavelength-division multiplexed channels separated by 100 GHz-wide stopbands, to parallelize several uncoupled MAC operations across the 5 THz telecommunications band, as has been done for crossbar arrays [6, 7, 9, 51]. This leads to a compute density of ~ 10 TMAC/s/mm², which is much better than MZI meshes and comparable with standard silicon microring crossbar arrays [51], with the added advantage of only $O(N)$ electronically controlled elements. We anticipate that future progress in modulation speed and power using high-confinement integrated photonic platforms will push these current estimates further, leading to experimental implementations of MAC operations using the architecture proposed here with improvements in complexity, speed, power and footprint.

ACKNOWLEDGMENTS

Funding: This work is supported by the U.S. Air Force Office of Scientific Research (FA9550-17-1-0002,

FA9550-18-1-0379). S. B. acknowledges the support of a Stanford Graduate Fellowship.

Competing interests: The authors declare no competing interests.

Data availability: The data related to this study is available in the manuscript and the supplementary materials. Additional data is available from the authors upon reasonable request.

REFERENCES

- [1] M. Reck, A. Zeilinger, H. J. Bernstein, and P. Bertani, “Experimental realization of any discrete unitary operator,” *Physical Review Letters*, vol. 73, no. 1, p. 58, 1994.
- [2] W. R. Clements, P. C. Humphreys, B. J. Metcalf, W. S. Kolthammer, and I. A. Walmsley, “Optimal design for universal multiport interferometers,” *Optica*, vol. 3, no. 12, pp. 1460–1465, 2016.
- [3] D. A. Miller, “Self-configuring universal linear optical component,” *Photonics Research*, vol. 1, no. 1, pp. 1–15, 2013.
- [4] J. Carolan, C. Harrold, C. Sparrow, E. Martín-López, N. J. Russell, J. W. Silverstone, P. J. Shadbolt, N. Matsuda, M. Oguma, M. Itoh, *et al.*, “Universal linear optics,” *Science*, vol. 349, no. 6249, pp. 711–716, 2015.
- [5] Y. Shen, N. C. Harris, S. Skirlo, M. Prabhu, T. Baehr-Jones, M. Hochberg, X. Sun, S. Zhao, H. Larochelle, D. Englund, *et al.*, “Deep learning with coherent nanophotonic circuits,” *Nature Photonics*, vol. 11, no. 7, p. 441, 2017.
- [6] A. N. Tait, M. A. Nahmias, B. J. Shastri, and P. R. Prucnal, “Broadcast and weight: an integrated network for scalable photonic spike processing,” *Journal of Lightwave Technology*, vol. 32, no. 21, pp. 4029–4041, 2014.
- [7] A. N. Tait, T. F. De Lima, E. Zhou, A. X. Wu, M. A. Nahmias, B. J. Shastri, and P. R. Prucnal, “Neuromorphic photonic networks using silicon photonic weight banks,” *Scientific reports*, vol. 7, no. 1, pp. 1–10, 2017.
- [8] J. Feldmann, N. Youngblood, C. Wright, H. Bhaskaran, and W. Pernice, “All-optical spiking neurosynaptic networks with self-learning capabilities,” *Nature*, vol. 569, no. 7755, pp. 208–214, 2019.
- [9] J. Feldmann, N. Youngblood, M. Karpov, H. Gehring, X. Li, M. L. Gallo, X. Fu, A. Lukashchuk, A. Raja, J. Liu, *et al.*, “Parallel convolution processing using an integrated photonic tensor core,” *arXiv preprint arXiv:2002.00281*, 2020.
- [10] X. Lin, Y. Rivenson, N. T. Yardimci, M. Veli, Y. Luo, M. Jarrahi, and A. Ozcan, “All-optical machine learning using diffractive deep neural networks,” *Science*, vol. 361, no. 6406, pp. 1004–1008, 2018.
- [11] S. Ohno, K. Toprasertpong, S. Takagi, and M. Takenaka, “Si microring resonator crossbar arrays for deep learning accelerator,” *Japanese Journal of Applied Physics*, vol. 59, no. SG, p. SGGE04, 2020.
- [12] S. T. Cundiff and A. M. Weiner, “Optical arbitrary waveform generation,” *Nature Photonics*, vol. 4, no. 11, p. 760, 2010.
- [13] V. Supradeepa, C. M. Long, R. Wu, F. Ferdous, E. Hamidi, D. E. Leaird, and A. M. Weiner, “Comb-based radiofrequency photonic filters with rapid tunability and high selectivity,” *Nature Photonics*, vol. 6, no. 3, p. 186, 2012.
- [14] M. Zhang, B. Buscaino, C. Wang, A. Shams-Ansari, C. Reimer, R. Zhu, J. M. Kahn, and M. Lončar, “Broadband electro-optic frequency comb generation in a lithium niobate microring resonator,” *Nature*, vol. 568, pp. 373–377, Apr. 2019.
- [15] H.-H. Lu, J. M. Lukens, N. A. Peters, O. D. Odele, D. E. Leaird, A. M. Weiner, and P. Lougovski, “Electro-optic frequency beam splitters and tritters for high-fidelity photonic quantum information processing,” *Physical Review Letters*, vol. 120, no. 3, p. 030502, 2018.
- [16] N. C. Menicucci, S. T. Flammia, and O. Pfister, “One-way quantum computing in the optical frequency comb,” *Physical Review Letters*, vol. 101, no. 13, p. 130501, 2008.
- [17] J. M. Lukens and P. Lougovski, “Frequency-encoded photonic qubits for scalable quantum information processing,” *Optica*, vol. 4, no. 1, pp. 8–16, 2017.
- [18] H.-H. Lu, A. M. Weiner, P. Lougovski, and J. M. Lukens, “Quantum Information Processing With Frequency-Comb Qudits,” *IEEE Photonics Technology Letters*, vol. 31, pp. 1858–1861, Dec. 2019.
- [19] C. Joshi, A. Farsi, S. Clemmen, S. Ramelow, and A. L. Gaeta, “Frequency multiplexing for quasi-deterministic heralded single-photon sources,” *Nature Communications*, vol. 9, no. 1, pp. 1–8, 2018.
- [20] J. Roslund, R. M. de Araújo, S. Jiang, C. Fabre, and N. Treps, “Wavelength-multiplexed quantum networks with ultrafast frequency combs,” *Nature Photonics*, vol. 8, pp. 109–112, Feb. 2014.
- [21] C. Reimer, S. Sciara, P. Roztocky, M. Islam, L. R. Cortés, Y. Zhang, B. Fischer, S. Loranger, R. Kashyap, A. Cino, S. T. Chu, B. E. Little, D. J. Moss, L. Caspani, W. J. Munro, J. Azaña, M. Kues, and R. Morandotti, “High-dimensional one-way quantum processing implemented on d-level cluster states,” *Nature Physics*, vol. 15, p. 148, Feb. 2019.
- [22] C. Joshi, A. Farsi, A. Dutt, B. Y. Kim, X. Ji, Y. Zhao, A. M. Bishop, M. Lipson, and A. L. Gaeta, “Frequency-Domain Quantum Interference with Correlated Photons from an Integrated Microresonator,” *Physical Review Letters*, vol. 124, p. 143601, Apr. 2020.
- [23] X. Zhu, C.-H. Chang, C. González-Arciniegas, J. Higgins, A. Pe’er, and O. Pfister, “Graph state engineering by phase modulation of the quantum optical frequency comb,” *arXiv preprint arXiv:1912.11215*, 2019.
- [24] Y. Hu, M. Yu, D. Zhu, N. Sinclair, A. Shams-Ansari, L. Shao, J. Holzgrafe, E. Puma, M. Zhang, and M. Lončar, “Reconfigurable electro-optic frequency shifter,” *arXiv preprint arXiv:2005.09621*, 2020.
- [25] L. Yuan, Q. Lin, M. Xiao, and S. Fan, “Synthetic dimension in photonics,” *Optica*, vol. 5, pp. 1396–1405, Nov. 2018.
- [26] T. Ozawa and H. M. Price, “Topological quantum matter in synthetic dimensions,” *Nature Reviews Physics*, vol. 1, pp. 349–357, Apr. 2019.
- [27] L. Yuan, Y. Shi, and S. Fan, “Photonic gauge potential in a system with a synthetic frequency dimension,” *Optics Letters*, vol. 41, pp. 741–744, Feb. 2016.
- [28] T. Ozawa, H. M. Price, N. Goldman, O. Zilberberg, and I. Carusotto, “Synthetic dimensions in integrated photonics: From optical isolation to four-dimensional quantum Hall physics,” *Physical Review A*, vol. 93, p. 043827, Apr. 2016.

- [29] B. A. Bell, K. Wang, A. S. Solntsev, D. N. Neshev, A. A. Sukhorukov, and B. J. Eggleton, "Spectral photonic lattices with complex long-range coupling," *Optica*, vol. 4, no. 11, pp. 1433–1436, 2017.
- [30] K. Wang, B. Bell, A. S. Solntsev, D. N. Neshev, B. J. Eggleton, and A. A. Sukhorukov, "Multidimensional synthetic chiral-tube lattices via nonlinear frequency conversion," *arXiv:2002.08591*, Feb. 2020.
- [31] A. Dutt, Q. Lin, L. Yuan, M. Minkov, M. Xiao, and S. Fan, "A single photonic cavity with two independent physical synthetic dimensions," *Science*, vol. 367, no. 6473, pp. 59–64, 2020.
- [32] C. Qin, F. Zhou, Y. Peng, D. Sounas, X. Zhu, B. Wang, J. Dong, X. Zhang, A. Alù, and P. Lu, "Spectrum control through discrete frequency diffraction in the presence of photonic gauge potentials," *Physical Review Letters*, vol. 120, no. 13, p. 133901, 2018.
- [33] A. Dutt, M. Minkov, Q. Lin, L. Yuan, D. A. Miller, and S. Fan, "Experimental band structure spectroscopy along a synthetic dimension," *Nature Communications*, vol. 10, no. 1, pp. 1–8, 2019.
- [34] L. Yuan, M. Xiao, Q. Lin, and S. Fan, "Synthetic space with arbitrary dimensions in a few rings undergoing dynamic modulation," *Physical Review B*, vol. 97, p. 104105, Mar. 2018.
- [35] D. M. Lukin, A. D. White, M. A. Guidry, R. Trivedi, N. Morioka, C. Babin, J. U. Hassan, N. T. Son, T. Ohshima, P. K. Vasireddy, *et al.*, "Spectrally reconfigurable quantum emitters enabled by optimized fast modulation," *arXiv preprint arXiv:2003.12591*, 2020.
- [36] H.-H. Lu, J. M. Lukens, B. P. Williams, P. Imany, N. A. Peters, A. M. Weiner, and P. Lougovski, "A controlled-NOT gate for frequency-bin qubits," *npj Quantum Information*, vol. 5, pp. 1–8, Mar. 2019.
- [37] M. Huhtanen and A. Perämäki, "Factoring matrices into the product of circulant and diagonal matrices," *Journal of Fourier Analysis and Applications*, vol. 21, no. 5, pp. 1018–1033, 2015.
- [38] D. Maclaurin, D. Duvenaud, and R. P. Adams, "Autograd: Effortless gradients in numpy," in *ICML 2015 AutoML Workshop*, vol. 238, 2015.
- [39] S. Molesky, Z. Lin, A. Y. Piggott, W. Jin, J. Vuckovic, and A. W. Rodriguez, "Outlook for inverse design in nanophotonics," *Nat. Photonics*, vol. 12, no. November, pp. 659–670, 2018.
- [40] M. Minkov, I. A. Williamson, L. C. Andreani, D. Gerace, B. Lou, A. Y. Song, T. W. Hughes, and S. Fan, "Inverse design of photonic crystals through automatic differentiation," *arXiv preprint arXiv:2003.00379*, 2020.
- [41] T. W. Hughes, I. A. D. Williamson, M. Minkov, and S. Fan, "Wave physics as an analog recurrent neural network," *Sci. Adv.*, vol. 5, no. 12, p. eaay6946, 2019.
- [42] R. H. Byrd, P. Lu, J. Nocedal, and C. Zhu, "A limited memory algorithm for bound constrained optimization," *SIAM Journal on scientific computing*, vol. 16, no. 5, pp. 1190–1208, 1995.
- [43] K. Fang, Z. Yu, and S. Fan, "Photonic aharonov-bohm effect based on dynamic modulation," *Physical Review Letters*, vol. 108, no. 15, p. 153901, 2012.
- [44] N. Tischler, C. Rockstuhl, and K. Słowik, "Quantum optical realization of arbitrary linear transformations allowing for loss and gain," *Physical Review X*, vol. 8, no. 2, p. 021017, 2018.
- [45] C. Wang, M. Zhang, B. Stern, M. Lipson, and M. Lončar, "Nanophotonic lithium niobate electro-optic modulators," *Opt. Express, OE*, vol. 26, pp. 1547–1555, Jan. 2018.
- [46] C. Wang, M. Zhang, X. Chen, M. Bertrand, A. Shams-Ansari, S. Chandrasekhar, P. Winzer, and M. Lončar, "Integrated lithium niobate electro-optic modulators operating at CMOS-compatible voltages," *Nature*, vol. 562, p. 101, Oct. 2018.
- [47] L. D. Tzuang, M. Soltani, Y. H. D. Lee, and M. Lipson, "High RF carrier frequency modulation in silicon resonators by coupling adjacent free-spectral-range modes," *Optics Letters*, vol. 39, pp. 1799–1802, Apr. 2014.
- [48] R. Van Laer, R. N. Patel, T. P. McKenna, J. D. Witmer, and A. H. Safavi-Naeini, "Electrical driving of X-band mechanical waves in a silicon photonic circuit," *APL Photonics*, vol. 3, p. 086102, Aug. 2018.
- [49] H. Tian, J. Liu, B. Dong, J. C. Skehan, M. Zervas, T. J. Kippenberg, and S. A. Bhave, "Hybrid integrated photonics using bulk acoustic resonators," *arXiv preprint arXiv:1907.10177*, 2019.
- [50] C. Reimer, Y. Hu, A. Shams-Ansari, M. Zhang, and M. Loncar, "High-dimensional frequency crystals and quantum walks in electro-optic microcombs," *arXiv preprint arXiv:1909.01303*, 2019.
- [51] M. A. Nahmias, T. F. de Lima, A. N. Tait, H.-T. Peng, B. J. Shastri, and P. R. Prucnal, "Photonic Multiply-Accumulate Operations for Neural Networks," *IEEE J. Sel. Top. Quantum Electron.*, vol. 26, pp. 1–18, Jan. 2020.
- [52] I. A. D. Williamson, T. W. Hughes, M. Minkov, B. Bartlett, S. Pai, and S. Fan, "Reprogrammable Electro-Optic Nonlinear Activation Functions for Optical Neural Networks," *IEEE J. Sel. Top. Quantum Electron.*, vol. 26, pp. 1–12, Jan. 2020.
- [53] X. Ji, X. Yao, Y. Gan, A. Mohanty, M. A. Tadayon, C. P. Hendon, and M. Lipson, "On-chip tunable photonic delay line," *APL Photonics*, vol. 4, p. 090803, Sept. 2019.
- [54] X. Ji, F. A. S. Barbosa, S. P. Roberts, A. Dutt, J. Cardenas, Y. Okawachi, A. Bryant, A. L. Gaeta, and M. Lipson, "Ultra-low-loss on-chip resonators with sub-milliwatt parametric oscillation threshold," *Optica*, vol. 4, pp. 619–624, June 2017.

SUPPLEMENTARY MATERIAL

I. Derivation of coupled-mode theory

Here, we derive the temporal coupled-mode theory formalism of Eqs. (1)-(3). We start with equation for the electric field $\mathbf{E}(\mathbf{r}, t)$ as derived from Maxwell's equations:

$$\nabla \times \nabla \times \mathbf{E}(\mathbf{r}, t) = \frac{1}{c^2} \frac{\partial^2}{\partial t^2} [(n(\mathbf{r})^2 + \delta\epsilon(\mathbf{r}, t))\mathbf{E}(\mathbf{r}, t)]. \quad (\text{S1})$$

Here, $n(\mathbf{r})$ is the time-independent refractive index of the ring-waveguide structure and $\delta\epsilon(\mathbf{r}, t)$ is the time-dependent dielectric constant change induced by the electro-optic modulators in the form

$$\delta\epsilon(\mathbf{r}, t) = \sum_{l=1}^{N_f} \delta\epsilon_l(\mathbf{r}) \cos(l\Omega_R t + \theta_l). \quad (\text{S2})$$

The modes of the unmodulated ring are separated by the free spectral range (FSR) $\Omega_R = c/n_g R$, where R is the radius of the ring and n_g is the group index of the waveguide forming the ring. In the presence of weak modulation, the electric field can be expanded in the basis of the unmodulated modes:

$$\mathbf{E}(\mathbf{r}, t) = \sum_m a_m(t) \mathbf{E}_m(\mathbf{r}) e^{i\omega_m t}, \quad (\text{S3})$$

where $a_m(t)$ are the time-dependent amplitudes and $\mathbf{E}_m(\mathbf{r})$ are the modal profiles for the m^{th} modes at frequencies $\omega_0 + m\Omega_R$. Substituting Eq. (S3) into Eq. (S1), we obtain

$$\begin{aligned} \sum_m a_m(t) e^{i\omega_m t} \nabla \times \nabla \times \mathbf{E}_m &= \frac{n^2}{c^2} \sum_m \mathbf{E}_m \left(\frac{\partial^2}{\partial t^2} a_m(t) e^{i\omega_m t} \right) \\ &+ \sum_{m,l} \frac{\delta\epsilon_l}{c^2} \mathbf{E}_m \left(\frac{\partial^2}{\partial t^2} a_m(t) e^{i\omega_m t} \cos(l\Omega_R t + \theta_l) \right) \end{aligned} \quad (\text{S4})$$

Using the fact that the unmodulated modes obey Maxwell's equations, i.e., $\nabla \times \nabla \times \mathbf{E}_m = (n^2(\mathbf{r})\omega_m^2/c^2)\mathbf{E}_m$ as well as the slowly varying envelope approximation where we ignore terms involving the second derivative of a_m , we obtain

$$2in^2 \sum_m \omega_m \mathbf{E}_m \partial_t a_m e^{i\omega_m t} - \sum_m \frac{\omega_m^2}{2} \sum_{l=1}^{N_f} \delta\epsilon_l (a_{m-l} \mathbf{E}_{m-l} e^{i\omega_m t + \theta_l} + a_{m+l} \mathbf{E}_{m+l} e^{i\omega_m t - \theta_l}) = 0. \quad (\text{S5})$$

Using the rotating wave approximation, taking a dot product with $\mathbf{E}_m^*(\mathbf{r})$ on both sides, and integrating with the normalization $\int \mathbf{E}_m^*(\mathbf{r}) \cdot \mathbf{E}_m(\mathbf{r}) d\mathbf{r} = \omega_m$, we get

$$-i\partial_t a_m = \sum_{l=1}^{N_f} \kappa_l a_{m-l} + \kappa_{-l} a_{m+l}, \quad (\text{S6})$$

where

$$\kappa_{\pm l} = -\frac{1}{4n^2} e^{\mp i\theta_l} \int \mathbf{E}_m^*(\mathbf{r}) \cdot \delta\epsilon_l(\mathbf{r}) \mathbf{E}_{m\pm l}(\mathbf{r}) d\mathbf{r} \quad (\text{S7})$$

$$\simeq -\frac{1}{4n^2} \int_0^{2\pi} e^{\mp i(l\phi + \theta_l)} \delta\epsilon_l(\phi) d\phi \int r^2 \sin\theta e^*(r, \theta) \delta\epsilon_l(r, \theta) e(r, \theta) dr d\theta \quad (\text{S8})$$

$$= -\frac{\alpha_l}{4n^2} \int_0^{2\pi} e^{\mp i(l\phi + \theta_l)} \delta\epsilon_l(\phi) d\phi, \quad (\text{S9})$$

with $\alpha_l = \int r^2 \sin\theta e^*(r, \theta) \delta\epsilon_l(r, \theta) e(r, \theta) dr d\theta$. Here we assume that all modes in the ring are of the form $E_m(\mathbf{r}) \simeq e(r, \theta) e^{-im\phi}$, i.e., the m -dependence of the modes under consideration of the unmodulated ring is predominantly from the azimuthal field profile.

II. Unitarity of Eq. (5)

The transformation implemented by the ring-waveguide system from the input ports \mathbf{s}^+ to the output ports \mathbf{s}^- is given by \mathcal{M} , where

$$\begin{aligned}\mathcal{M} &= \mathcal{I} + i\sqrt{2\Gamma}[\Delta\omega - i\Gamma - \mathcal{K}]^{-1}\sqrt{2\Gamma} \\ &= \mathcal{I} + 2i\left[\Delta\omega\Gamma^{-1} - i\mathcal{I} - \sqrt{\Gamma^{-1}}\mathcal{K}\sqrt{\Gamma^{-1}}\right]^{-1}\end{aligned}\quad (\text{S10})$$

$$= \mathcal{I} + 2i\left[\Delta\omega\Gamma^{-1} - i\mathcal{I} - \tilde{\mathcal{K}}\right]^{-1}\quad (\text{S11})$$

where $\tilde{\mathcal{K}} = \sqrt{\Gamma^{-1}}\mathcal{K}\sqrt{\Gamma^{-1}}$. To show that \mathcal{M} is unitary, we write the first term of Eq. (S11) as $\mathcal{I} = \left[\Delta\omega\Gamma^{-1} - i\mathcal{I} - \tilde{\mathcal{K}}\right]\left[\Delta\omega\Gamma^{-1} - i\mathcal{I} - \tilde{\mathcal{K}}\right]^{-1}$, obtaining

$$\mathcal{M} = \left[\Delta\omega\Gamma^{-1} + i\mathcal{I} - \tilde{\mathcal{K}}\right]\left[\Delta\omega\Gamma^{-1} - i\mathcal{I} - \tilde{\mathcal{K}}\right]^{-1}\quad (\text{S12})$$

By writing the first term of Eq. (S11) as $\mathcal{I} = \left[\Delta\omega\Gamma^{-1} - i\mathcal{I} - \tilde{\mathcal{K}}\right]^{-1}\left[\Delta\omega\Gamma^{-1} - i\mathcal{I} - \tilde{\mathcal{K}}\right]$ we get another equivalent expression for \mathcal{M} as

$$\mathcal{M} = \left[\Delta\omega\Gamma^{-1} - i\mathcal{I} - \tilde{\mathcal{K}}\right]^{-1}\left[\Delta\omega\Gamma^{-1} + i\mathcal{I} - \tilde{\mathcal{K}}\right]\quad (\text{S13})$$

To verify that \mathcal{M} is unitary, we use the expression for \mathcal{M} from Eq. (S12) and for \mathcal{M}^\dagger from Eq. (S13):

$$\begin{aligned}\mathcal{M}^\dagger\mathcal{M} &= \left[\Delta\omega\Gamma^{-1} - i\mathcal{I} - \tilde{\mathcal{K}}\right]\left[\Delta\omega\Gamma^{-1} + i\mathcal{I} - \tilde{\mathcal{K}}\right]^{-1}\left[\Delta\omega\Gamma^{-1} + i\mathcal{I} - \tilde{\mathcal{K}}\right]\left[\Delta\omega\Gamma^{-1} - i\mathcal{I} - \tilde{\mathcal{K}}\right]^{-1} \\ &= \left[\Delta\omega\Gamma^{-1} - i\mathcal{I} - \tilde{\mathcal{K}}\right]\mathcal{I}\left[\Delta\omega\Gamma^{-1} - i\mathcal{I} - \tilde{\mathcal{K}}\right]^{-1} \\ &= \mathcal{I}.\end{aligned}\quad (\text{S14})$$

In this derivation, we have used the fact that \mathcal{K} is Hermitian for a real refractive-index modulation $\delta\epsilon(\mathbf{r}, t)$ and that Γ is Hermitian.

III. Truncation of modes in the synthetic frequency dimension

A ring resonator with a large circumference $L = 2\pi R$ supports a large number of resonant modes spaced approximately equally by the FSR. To achieve the high fidelities presented in this work, it is necessary to truncate the number of modes into which the input photons can couple so as to prevent the leakage of photons into undesired modes outside the $2N_{\text{sb}} + 1$ -mode-wide band of interest. Here, we discuss in detail one method to achieve this truncation and numerically show its performance using a scattering matrix (S-matrix) analysis. For this purpose, consider a small auxiliary ring of length L_1 coupled to the main ring with a frequency-independent strength t_1 , as shown in Fig. S1(a). We first discuss the unmodulated system. The S-matrices linking the fields at various points in the ring can be written as

$$\begin{pmatrix} a_3 \\ a_4 \end{pmatrix} = S_0 \begin{pmatrix} a_1 \\ a_2 \end{pmatrix}\quad (\text{S15})$$

$$\begin{pmatrix} a_2 e^{-i\theta_0/2} \\ a_6 e^{-i\theta_1} \end{pmatrix} = S_1 \begin{pmatrix} a_5 e^{i\theta_0/2} \\ a_6 \end{pmatrix}\quad (\text{S16})$$

where $\theta_0 = \beta(\omega)L + i\alpha L$ incorporates the effect of phase accumulation and amplitude attenuation as light propagates around the ring and $\theta_1 = \beta(\omega)L_1 + i\alpha L_1$ describes similar effects in the auxiliary ring. α is the propagation loss per unit length such that $\alpha L/T_R = \gamma_i$, where $T_R = 2\pi/\Omega_R$ is the round-trip time. The matrices S_0 and S_1 , which describe the directional couplers coupling the main ring to the external waveguide and to the auxiliary ring, respectively, have the form:

$$S_0 = \begin{pmatrix} \sqrt{1-t_e^2} & it_e \\ it_e & \sqrt{1-t_e^2} \end{pmatrix}; \quad S_1 = \begin{pmatrix} \sqrt{1-t_1^2} & it_1 \\ it_1 & \sqrt{1-t_1^2} \end{pmatrix}\quad (\text{S17})$$

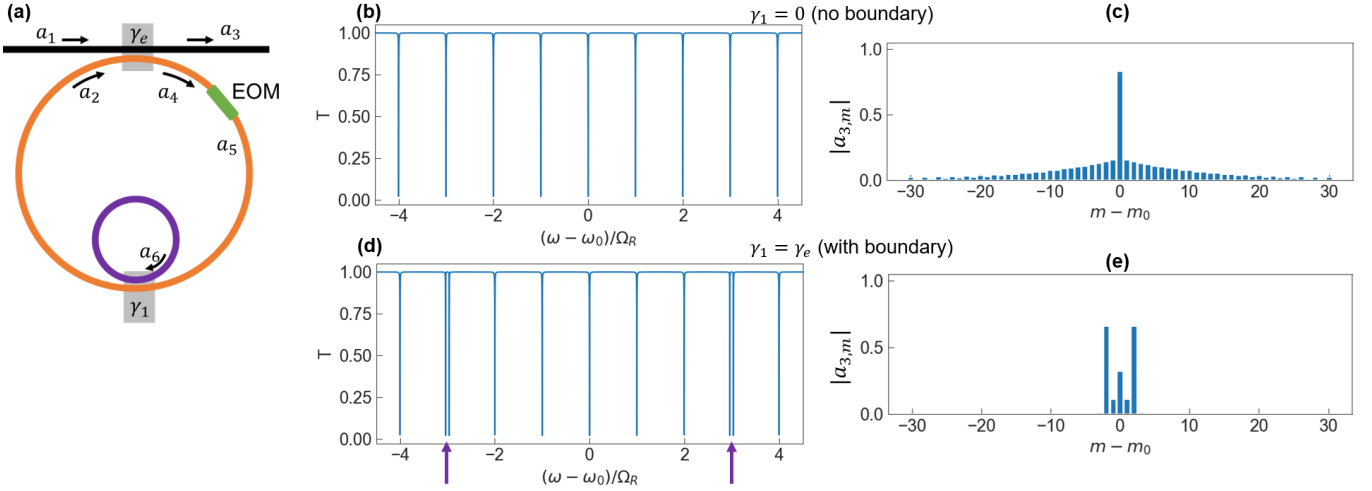


FIG. S1. Construction of boundaries in synthetic dimensions using auxiliary rings. (a) Schematic for S-matrix calculations, showing fields at various locations within the resonator. The ring-waveguide coupling is $\gamma_e = t_e^2/2T_R$, and the coupling between the main ring and the auxiliary ring is $\gamma_1 = t_1^2/2T_R$. The length of the main and auxiliary rings are L and L_1 respectively. (b) Steady-state transmission spectrum of the unmodulated ring without coupling to the auxiliary ring ($t_1 = 0$). Uniformly spaced modes separated by Ω_R are seen. (c) Output spectrum for a modulated ring excited by a single input frequency at mode m_0 with no boundary $t_1 = 0$. The input spreads out into a large number of frequency modes since there is no boundary. (d) and (e) Same as (b) and (c) but with a boundary at modes $\omega_0 \pm 3\Omega_R$, created by choosing $L_1 = L/6$ and $t_1 = t_e$. In (d), the ± 3 modes are split by the coupling to the auxiliary ring, as indicated by the purple arrows. In (e), we see that the output spectrum is localized to the five modes centered around m_0 , since the modulation at the FSR is not able to couple across the boundary. 99.98% of the input power stays within the five modes defined by the boundaries. Note that in (b) and (d) we used an intrinsic loss $\gamma_i = \gamma_e$ for ease of visualization of resonant dips in transmission. In (c) and (e) we choose $\gamma_e \gg \gamma_i$.

In the absence of modulation, $a_5 = a_4$. For a single frequency continuous wave excitation, we can solve Eqs. (S15) and (S16) by assuming $a_1 = 1$ and calculating a_3 . The transmission spectrum T at the through-port of the ring is plotted in Fig. S1(b) and (d) without ($t_1 = 0$) and with ($t_1 = t_e$) the auxiliary ring, respectively. Without the auxiliary ring, the modes are equally spaced, showing resonances for $(\omega - \omega_0)/\Omega_R$ being an integer. In the presence of an auxiliary ring with a length $L_1 = L/6$, every sixth mode is split into a doublet. Hence, a set of 5 modes are equally spaced, which can be coupled by the modulation at the FSR, but the split doublets at every sixth mode cannot be coupled by the modulation. This creates a one-mode boundary separating sets of 5 modes. We confirmed in our simulations that boundaries consisting of a larger number of modes can be formed by choosing a non-integer L_1/L and/or by using additional auxiliary rings. Note that for these calculations we assumed an intrinsic loss rate $\gamma_i = \gamma_e$ only to observe resonant dips in the transmission, but for high fidelity linear transformations, we set $\gamma_e \gg \gamma_i$, i.e. the ring is strongly over-coupled to the external waveguide. In this case, the transmission spectrum is near unity for both on and off resonance, but there are large on-resonance group delays.

In the presence of modulation, the fields a_5 and a_4 are coupled by the electro-optic modulator. In this case, each of the fields consists of multiple frequency components denoted as Floquet side bands, where the frequency of the Floquet sidebands are determined both by the input frequency ω_{in} and the modulation frequency Ω_{mod} : $\omega'_m = \omega_{\text{in}} + m\Omega_{\text{mod}}$. Thus, the propagation phases $\theta_0(\omega)$ and $\theta_1(\omega)$ are dependent on the order of the Floquet sideband. The relation between the fields before and after the modulator in the S-matrix formalism can be obtained by exponentiating the \mathcal{K} matrix (see the discussion around Eq. (4) in the main text) from the coupled-mode theory:

$$S_K = e^{i\mathcal{K}T_R} \quad (\text{S18})$$

$$a_{5,m} = \sum_n [S_K]_{m,n} a_{4,n} \quad (\text{S19})$$

Using a large enough number of Floquet sidebands for calculations, the form of the matrix S_K for a single modulation

frequency $\Omega_{\text{mod}} = \Omega_{\text{R}}$ (such that only κ_1 is nonzero) is:

$$S_K \approx \begin{pmatrix} \ddots & \vdots & \vdots & \vdots & \\ \cdots & J_0(\kappa_1 T_R) & J_1(\kappa_1 T_R) & J_2(\kappa_1 T_R) & \cdots \\ \cdots & J_{-1}(\kappa_1 T_R) & J_0(\kappa_1 T_R) & J_1(\kappa_1 T_R) & \cdots \\ \cdots & J_{-2}(\kappa_1 T_R) & J_{-1}(\kappa_1 T_R) & J_0(\kappa_1 T_R) & \cdots \\ & \vdots & \vdots & \vdots & \ddots \end{pmatrix} \quad (\text{S20})$$

Using such a construction, we can calculate the steady state output frequency content for a certain input. In particular, we can check if the creation of boundaries in the synthetic dimension restricts the propagation of light to within the bounded set of modes without causing additional loss. We show this in Fig. S1(c) and (e) for the cases without a boundary and with a boundary respectively. In the absence of coupling to the auxiliary ring, the input at m_0 spreads out into a large number of modes (Fig. S1(c)), whereas in the presence of the boundary created by coupling to the auxiliary ring, 99.98% of the power stays localized within the 5 modes of interest (Fig. S1(e)). As in the unmodulated case, we checked that this behavior can be extended for multiple modulation tones by using non-integer values of L_1/L and/or by using additional auxiliary rings.

IV. Parameters of the optimized systems

In this section, we list the parameters κ_l/γ found by the inverse-design algorithm that we use in Figs. 2-6.

Fig. 2(b)	Ring 1	Ring 2
κ_1/γ	$1.3508e^{0.2499\pi}$	$3.8269e^{0.2500\pi}$
κ_2/γ	$2.3574e^{i0.0\pi}$	$0.4878e^{i\pi}$

Fig. 3	Ring 1	Ring 2	Ring 3
κ_1/γ	$0.39e^{i0.3334\pi}$	$0.1469e^{i0.3331\pi}$	$0.6757e^{i0.3334\pi}$
κ_2/γ	$0.0001e^{i0.0\pi}$	$0.5152e^{i0.1666\pi}$	$0.0144e^{i0.1661\pi}$
κ_3/γ	$1.1031e^{i0.0\pi}$	$0.359e^{i0.0\pi}$	$1.0308e^{i0.0\pi}$

Fig. 4(c)	Ring 1
κ_1/γ	$0.9992e^{i0.5004\pi}$
κ_2/γ	$0.9990e^{-i0.5004\pi}$
κ_3/γ	$0.9999e^{i0.5004\pi}$
κ_4/γ	$0.9992e^{-i0.4996\pi}$

Fig. 5(c)	Ring 1	Ring 2	Ring 3	Ring 4
κ_1/γ	$0.5937e^{i0.2269\pi}$	$0.4273e^{i0.5323\pi}$	$0.8302e^{i0.3744\pi}$	$0.3750e^{i0.2093\pi}$
κ_2/γ	$0.5712e^{i0.3739\pi}$	$1.1299e^{i0\pi}$	$0.3310e^{i0\pi}$	$0.6499e^{i0.3417\pi}$
κ_3/γ	$0.8369e^{i0.2066\pi}$	$0.5694e^{-i0.6669\pi}$	$0.6474e^{-i0.6793\pi}$	$0.3388e^{i0.0561\pi}$
κ_4/γ	$1.4019e^{i0.3548\pi}$	$0.0756e^{i0.0\pi}$	$0.2493e^{-i0.776\pi}$	$1.0957e^{i0.0814\pi}$

Fig. 6	Ring 1	Ring 2	Ring 3	Ring 4
κ_1/γ	$0.6023e^{i0.6613\pi}$	$0.9449e^{i0.4425\pi}$	$0.1696e^{-i0.6438\pi}$	$1.208e^{i0.481\pi}$
κ_2/γ	$0.145e^{i0.9533\pi}$	$0.3338e^{-i0.8814\pi}$	$0.2973e^{i0.0\pi}$	$0.2441e^{-i0.2564\pi}$
κ_3/γ	$0.8391e^{-i0.3493\pi}$	$0.8065e^{-i0.954\pi}$	$0.4546e^{i0.4662\pi}$	$1.0546e^{i0.2438\pi}$
κ_4/γ	$0.4252e^{-i0.3689\pi}$	$1.7639e^{i0.1285\pi}$	$1.0045e^{i0.7818\pi}$	$0.6614e^{i0.6218\pi}$